Indian J Phys
https://doi.org/10.1007/s12648-024-03517-5

ORIGINAL PAPER

Investigation of the structural, electronic and optical properties of halide perovskites $AgXBr_3$ (X = Ca, Sr, and Ba) using DFT framework

D Allali[1,2], A Bedjaoui[3]*, A Bouhemadou[4], B Deghfel[5], M Radjai[6], S S Essaoud[7], H Allaf[6], A Benmakhlouf[8] and Y Al-Douri[9,10,11]

[1]Laboratory of Materials and Renewable Energy, Faculty of Sciences, University Pole, Road Bordj Bou Arreridj, 28000 M'sila, Algeria

[2]Department of Technology, Faculty of Technology, University Pole, Road Bordj Bou Arreridj, 28000 M'sila, Algeria

[3]Department of Technology, Faculty of Technology, University of Bejaia, 6000 Bejaia, Algeria

[4]Laboratory for Developing New Materials and Their Characterizations, Department of Physics, Faculty of Science, Ferhat Abbas University - Setif 1, 19000 Setif, Algeria

[5]Laboratory of Materials and Renewable Energy, Faculty of Sciences, Mohamed Boudiaf University of M'sila, 28000 M'sila, Algeria

[6]Laboratory of Physics of Experimental Techniques and Their Applications, University of Medea, 26000 Medea, Algeria

[7]Department of Physics, Faculty of Science, University of M'sila, 28000 M'sila, Algeria

[8]Laboratoire des Matériaux Pour Application et Valorisation des Énergies Renouvelables (LMAVER), Université Amar Telidji de Laghouat, BP37G, 03000 Laghouat, Algeria

[9]College of Health and Medical Techniques, Al-Bayan University, Baghdad, Iraq

Nanotechnology and Catalysis Research Center (NANOCAT), University of Malaya, 50603 Kuala Lumpur, Malaysia

Department of Mechanical Engineering, Faculty of Engineering, Piri Reis University, Eflatun Sk. No: 8, 34940 Tuzla, Istanbul, Turkey

Received: 17 June 2024 / Accepted: 12 December 2024

Abstract: Using the full-potential linearised augmented plane wave approach, we examined the structural, electronic, and optical features of $AgXBr_3$ perovskite materials (X = Ca, Sr, or Ba). The GGA-PBEsol exchange-correlation functional yields equilibrium structure parameters that match the literature. Electronic structure analysis demonstrates that the Tran–Blaha modified Becke–Johnson and screened hybrid HSE06 functionals widen the bandgap compared to GGA-PBEsol. As X's atomic size rises, its indirect fundamental bandgap lowers. The density of states diagrams, complex dielectric function, electronic energy loss function, absorption coefficient, reflectivity, extinction coefficient, and refractive index were thoroughly explored. Results show that reducing the bandgap increases the dielectric function's zero frequency limits. Origins of optical spectra peaks and characteristics have been identified.

Keywords: Halide perovskites; FP-LAPW method; Structural parameters; Optoelectronic characteristics; Electronic transition energy

1. Introduction

Inorganic halide perovskites have garnered significant attention due to their unique properties and their implication in diverse applications. The recent integration of ABX_3 halide perovskite materials as photoabsorbers has revolutionized photovoltaic solar cells, leading to a remarkable increase in power conversion efficiency from approximately 3.8% in 2009 to nearly 25% in 2019 [1–5]. Moreover, the applications of these materials extend beyond photovoltaics; they are also exploited in photodetectors, batteries and LEDs [6, 7]. The flexibility of perovskites in terms of composition allows for the creation of

Supplementary Information The online version contains supplementary material available at https://doi.org/10.1007/s12648-024-03517-5.

*Corresponding author, E-mail: abdelhak.bedjaoui@univ-bejaia.dz

Published online: 07 January 2025

a wide range of new structures. This versatility gives rise to a broad spectrum of novel chemical and physical properties [8], rendering them a highly significant category of functional materials. These materials have been extensively studied and applied in numerous fields, including ferroelectricity [9–12], piezoelectricity [9, 13], ceramic science [14, 15], photovoltaics [3, 16–19]

One of the most ranges of these materials is the halide perovskites ABX_3, where X represents halides like F, Cl, Br, or I. These compounds have attracted significant attention in the fields of technology and science because of their exceptional optical, electrical, and magnetic properties, as well as their cost-effective manufacturing process [8, 16, 20–25]. They are increasingly being utilized in solar cells, optical fibers, solid-state lubricants, thin-film electrolytes, lasers, thermoelectrics, and other applications that exploit their piezoelectric, optoelectronic, photochemical, and photoluminescent properties [24, 26–33].

In recent work, Gómez-Peralta and Bokhimi [34] employed Artificial Neural Networks (ANN) [35] to predict the properties of a series of halide perovskites. The $AgXBr_3$compounds, where X are Ca, Sr, or Ba, are among the aforementioned predicted halide perovskites. These three compounds have been predicted to crystalize in their idealized cubic form, with space group $Pm\bar{3}m$ (no. 221). The unit cell of this structure contains one unit formula (Z = 1), with the atomic positions defined by their Wyckoff sites: Ag: 1*a* (0, 0, 0), X (X = Ca, Sr, Ba): 1*b* (1/2, 1/2, 1/2), and Br: 3*c* (1/2, 1/2, 0). The predicted unit cell parameters for $AgCaBr_3$, $AgSrBr_3$, and $AgBaBr_3$ are 5.4815 Å, 5.7490 Å, and 6.1310 Å, respectively. Their expected bandgap energies are 0.73 eV for $AgCaBr_3$ and $AgSrBr_3$, and 0.64 eV for $AgBaBr_3$ [34]. As of now, the $AgXBr_3$ compounds, with X representing Ca, Sr, or Ba, have neither been synthesized nor subjected to experimental study. Building on previous research, our study aims to explore the structural, electronic and optical properties of these three lead-free halide perovskites ($AgXBr_3$, X = Ca, Sr, Ba) as promising eco-friendly materials. To achieve a comprehensive understanding of their properties, we utilized the full-potential linearized augmented plane wave (FP-LAPW) method, implemented in the WIEN2K code [36], along with the recently developed Tran–Blaha modified Becke–Johnson (TB-mBJ) exchange–correlation potential[37] for better describing the electronic structure. This advanced computational technique enables us to provide a detailed analysis of these materials' properties, paving the way for future experimental studies and eventual interesting applications.

2. Computational methodology

The full potential linearized augmented plane wave plus local orbitals (FP-LAPW + lo) approach [38], as implemented in the WIEN2k package [36], was utilized to perform all first-principles computations. In the FP-LAPW approach, the electronic wave functions are described through a linear combination of radial atomic functions and their energy derivatives, multiplied by spherical harmonics inside the non-overlapping muffin-tin spheres (MTS) of radii R_{MT}, which are centered at atomic sites, while the electronic wave functions in the interstitial region (IR) are developed on a plane wave basis set. The spherical functions are constrained by a cutoff value $l_{\max}$, whereas the plane wave basis set is constrained by a cutoff parameter: $R_{min}^{MT}K_{max}$, where K_{max} represents the maximum plane wave vector in the *k*-space and R_{min}^{MT} represents the minimum muffin-tin radius. In this study, the value of $l_{\max}$ was chosen to be 10, whereas the value of $R_{min}^{MT}K_{max}$ was chosen to be 7. In this study, a $10 \times 10 \times 10$ Monkhorst–Pack grid [39] was employed to sample the first Brillouin zone. The self-consistent field iteration technique was then executed until the crystal's total energy reached a convergence value of 10^{-5} Ry. The electronic exchange–correlation effects were simulated using the well-known PBEsol variant of the generalized gradient approximation, called [40] in order to examine the structural properties. Conventional GGA is known for its propensity to underestimate the band gap value. Thus, to better determine the bandgap values of the examined materials, the Tran–Blaha modified Becke–Johnson (TB-mBJ) potential [37] and the screened hybrid functional HSE06 [41–43] were employed to model the exchange–correlation interactions for the electronic structure evaluation.

The optical properties calculation package of the WIEN2k code [36] was used to calculate the optical properties of the considered compounds. The calculation of the imaginary part $(\varepsilon_2(\omega))$ of the dielectric function $(\varepsilon(\omega) = \varepsilon_1(\omega) + i\varepsilon_2(\omega))$ involves summing the direct electronic transitions between occupied states in the valence band and unoccupied states in the conduction band. The exclusion of indirect and intraband transitions from the summing was based on their minimal impact on semiconductors and insulators. The Kramers–Kronig transformation [44] was used to calculate the real component $(\varepsilon_1(\omega))$. The density of states and optical coefficients, including absorption coefficient, refractive index, extinction coefficient, reflectivity coefficient, and electronic loss-energy function, were calculated using $21 \times 21 \times 21$ Monkhorst–Pack *k*-points.

3. Results and discussion

3.1. Structural properties

The perovskite materials $AgXBr_3$ (X = Ca, Sr, and Ba) have a simple cubic crystal structure, characterized by the space group $Pm\bar{3}m$ (#221) [34]. The unit cell comprises one chemical formula unit (Z = 1). The atomic positions within the unit cell are as follows: Ag occupies the Wyckoff site 1*a* (0, 0, 0), X (X = Ca, Sr, and Ba) resides in the Wyckoff site 1*b* (1/2, 1/2, 1/2), and Br is located in the Wyckoff site 3*c* (1/2, 1/2, 0). Figure 1 depicts the prototype unit cell of $AgCaBr_3$. The Ca cation is coupled with six Br anions, resulting in the formation of regular octahedra $CaBr_6$, and Ag cation exhibit coordination with twelve bromine anions, resulting in the formation of cuboctahedral coordination environments. To ascertain the lattice parameter (*a*), bulk modulus (*B*), and its pressure derivative (*B*') for the considered compounds, we employed the Birch and Birch-Murnaghan equations of state (EOS) [45] to fit the calculated total energy (*E*) against the unit cell volume (*V*). The calculated values of the equilibrium lattice parameter (*a*), bulk modulus (*B*) and its pressure derivative (*B*') for $AgCaBr_3$, $AgSrBr_3$, and $AgBaBr_3$ are listed in Table 1. It is observed that the lattice parameter values, exhibit a satisfactory level of concurrence with the existing data documented in the literature [34]. It is worth mentioning that the lattice parameter of $AgXBr_3$ increases as the atomic size of X element increases. A comparison of the bulk modulus values listed in Table 1 for the three compounds studied shows that they decrease when moving from $AgCaBr_3$ to $AgSrBr_3$ and then to $AgBaBr_3$. This trend suggests that the hardness of these compounds decreases slightly when moving from $AgCaBr_3$ to $AgSrBr_3$ and then to $AgBaBr_3$. We note that the values of B acquired by the two equations of state, namely Birch and Birch-Murnaghan EOS, are in excellent agreement, indicating the reliability of the results obtained.

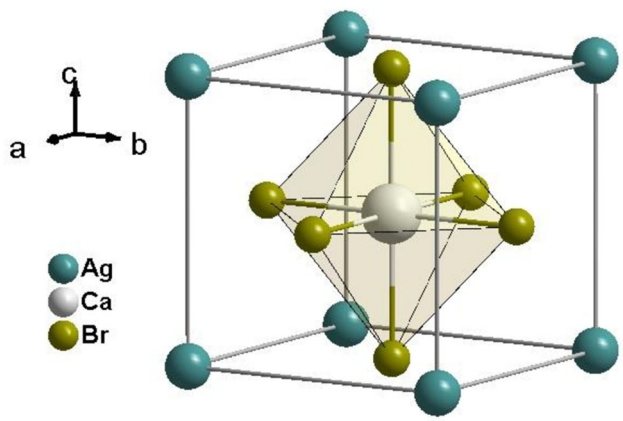

Fig. 1 Schematic representation of the unit cell of $AgCaBr_3$ showing the $CaBr_6$ octahedron

To evaluate the stability of the materials under consideration with the cubic structure, we computed the Goldsmith tolerance factor (*t*) [46]. The stability of a cubic perovskite ABX_3 structure is conditioned by values of "*t*" between 0.8 and 1.0. The Goldschmidt tolerance factor values for $AgCaBr_3$, $AgSrBr_3$, and $AgBaBr_3$, as shown in Table 1, fall within the required values range. This suggests that these materials exhibit stability within the cubic structure.

Furthermore, we calculated the formation enthalpy (ΔH) and cohesive energy (E_{coh}) for $AgCaBr_3$, $AgSrBr_3$, and $AgBaBr_3$ in order to assess their structural and thermodynamic stabilities [47–51]. The formation enthalpies and cohesive energies of the compounds $AgXBr_3$ (X = Ca, Sr and Ba) were calculated using the subsequent relationships:

$$\Delta H = \frac{1}{n_{Ag} + n_X + n_{Br}} \left[E_{tot}^{AgXBr_3} - \left(n_{Ag} E_{tot}^{Ag(solid)} + n_X E_{tot}^{X(solid)} + n_{Br} E_{tot}^{Br(solid)} \right) \right]$$

$$E_{coh} = \frac{1}{n_{Ag} + n_X + n_{Br}} \left[E_{tot}^{AgXBr_3} - \left(n_{Ag} E_{tot}^{Ag(atom)} + n_X E_{tot}^{X(atom)} + n_{Br} E_{tot}^{Br(atom)} \right) \right]$$

Here, $E_{tot}^{AgXBr_3}$ is the total energy of the primitive cell of $AgXBr_3$; $E_{tot}^{Ag(solid)}$,$E_{tot}^{X(solid)}$ and $E_{tot}^{Br(solid)}$ are the total energies per atom of the pure Ag, X (X = Ca, Sr, Ba) and Br elements in their solid state; $E_{tot}^{Ag(atom)}$, $E_{tot}^{X(atom)}$ and $E_{tot}^{Br(atom)}$ are the total energies of the isolated Ag, X, and Br atoms; n_{Ag}, n_X and n_{Br} represent respectively the number of Ag, X, and Br atoms in the primitive cell. The calculated formation enthalpies and cohesive energies for $AgXBr_3$ (X = Ca, Sr, Ba) are given in Table 1. The studied perovskites in their cubic structure are structurally and energetically stable, as evidenced by the negative values of both the formation enthalpies (ΔH) and cohesive energies (E_{coh}). Figure 2 depicts the fluctuation of ΔH in relation to pressure. It is evident that the value of ΔH remains negative within the specified pressure range, but it rises as the pressure increases. Consequently, the stability of these materials decreases as pressure increases. It is also observed that the stability of $AgXBr_3$ decreases as the cation X moves down the column of the periodic table, in the order: Ca → Sr → Ba.

To assess the dynamical stability of the compounds under scrutiny, we examined their phonon dispersion spectra. This examination was carried out employing the linear response method implemented in the CASTEP code [52]. The resulting phonon dispersion diagrams are

Table 1 Calculated lattice parameter (a_0, in Å), Goldschmidt tolerance factor (t), cohesive energy (E_{coh}, in eV/atom), formation enthalpy (ΔH, in eV/atom), bulk modulus (B, in GPa), bulk modulus first pressure derivative (B') for the ternary halide perovskites: $AgCaBr_3$, $AgSrBr_3$ and $AgBaBr_3$

Property	$AgCaBr_3$		$AgSrBr_3$		$AgBaBr_3$	
	GGA	Other [34]	GGA	Other [34]	GGA	Other [34]
a_0	5.6201	5.4815	5.9082	5.7490	6.2453	6.1310
t	0.86		0.80		0.79	
E_{coh}	− 1.2288		− 1.1965		− 1.2014	
ΔH	− 1.3925		− 1.3803		− 1.3409	
B	21.17[1]		17.66[1]		14.62[1]	
B'	21.17[2]		17.66[2]		14.62[2]	
	4.52[1]		4.58[1]		4.63[1]	
	4.53[2]		4.58[2]		4.64[2]	

[1]from Birch E—V EOS, [2]from Birch-Murnaghan E—V EOS

visualized in Fig. 3. In materials research, the absence of soft modes (also referred to as imaginary modes or negative frequencies) in the phonon dispersion curve of a material is an indicator of its dynamic stability [53–59]. Theoretically, soft modes represented by negative frequencies in the phonon dispersions of materials indicate their dynamic instability. Such soft modes are known to initiate lattice instability, potentially leading to structural phase transitions. Additionally, their presence suggests that synthesizing the compound under normal conditions may be challenging. It is, however, imperative to emphasize the nuanced nature of the implications associated with the presence of negative frequencies in the phonon dispersion curves of materials. In some cases, this phenomenon does not categorically mean that the crystal structures of these materials are inherently unstable. Indeed, a multitude of previously synthesized materials exhibited soft vibrational modes [60–62], thus demonstrating that a material can maintain its stability even in the presence of these soft modes. Therefore, the mere existence of soft modes within the materials in question should not be automatically interpreted as proof of the impossibility of their synthesis. Further investigations are needed to determine the conditions under which the considered materials can be synthesized and stabilized.

To examine the impact of external pressure on the unit cell volume "V" and lattice parameter "a" of the $AgXBr_3$ (X = Ca, Sr, and Ba) materials, we examined a/a_0 and V/V_0 as functions of pressure as depicted in Fig. 4, where V and a represent the unit cell volume and lattice parameter, respectively, at a pressure P, while V_0 and a_0 denote their respective values at zero pressure. The calculated a/a_0 and V/V_0 ratios as functions of pressure were well fitted, as illustrated in Fig. 4, by the following third-order polynomials:

$$\begin{cases} \left(\frac{a}{a_0}\right)^{AgCaBr_3} = 1 - 0.014P + 7.41 \times 10^{-4}P^2 - 1.91 \times 10^{-5}P^3 \\ \left(\frac{V}{V_0}\right)^{AgCaBr_3} = 1 - 0.040P + 2.39 \times 10^{-3}P^2 - 6.33 \times 10^{-5}P^3 \end{cases},$$

$$\begin{cases} \left(\frac{a}{a_0}\right)^{AgSrBr_3} = 1 - 0.016P + 9.27 \times 10^{-4}P^2 - 2.48 \times 10^{-5}P^3 \\ \left(\frac{V}{V_0}\right)^{AgSrBr_3} = 1 - 0.046P + 2.96 \times 10^{-3}P^2 - 8.11 \times 10^{-5}P^3 \end{cases},$$

$$\begin{cases} \left(\frac{a}{a_0}\right)^{AgBaBr_3} = 1 - 0.018P + 1.16 \times 10^{-3}P^2 - 3.22 \times 10^{-5}P^3 \\ \left(\frac{V}{V_0}\right)^{AgBaBr_3} = 1 - 0.053P + 3.65 \times 10^{-3}P^2 - 1.03 \times 10^{-4}P^3 \end{cases}$$

It is clear from Fig. 4 that both a/a_0 and V/V_0 decrease with increasing pressure for $AgXBr_3$ (X = Ca, Sr, Ba). In addition, it is found that the resistance to both unidirectional and volumetric compression decreases in the order of $AgCaBr_3$, $AgSrBr_3$, and $AgBaBr_3$, with $AgBaBr_3$ being the most compressible.

3.2. Electronic properties

The electronic structure of a substance is intricately linked to several of its physical characteristics, including optical, transport, and thermoelectric characteristics. The electronic band structure and density of states of $AgXBr_3$ (X = Ca, Sr, and Ba) compounds were extensively investigated in this study. The energy band dispersions along the X–R–M–Γ–R path in the first Brillouin zone for the materials under consideration were determined using the GGA-PBEsol, TB-mBJ and HSE06 exchange–correlation functionals. Figure 5 displays the computed energy band dispersions using the GGA-PBEsol and TB-mBJ functionals. The calculated bandgap values for herein studied compounds within the GGA-PBE, TB-mBJ and HSE06 exchange–

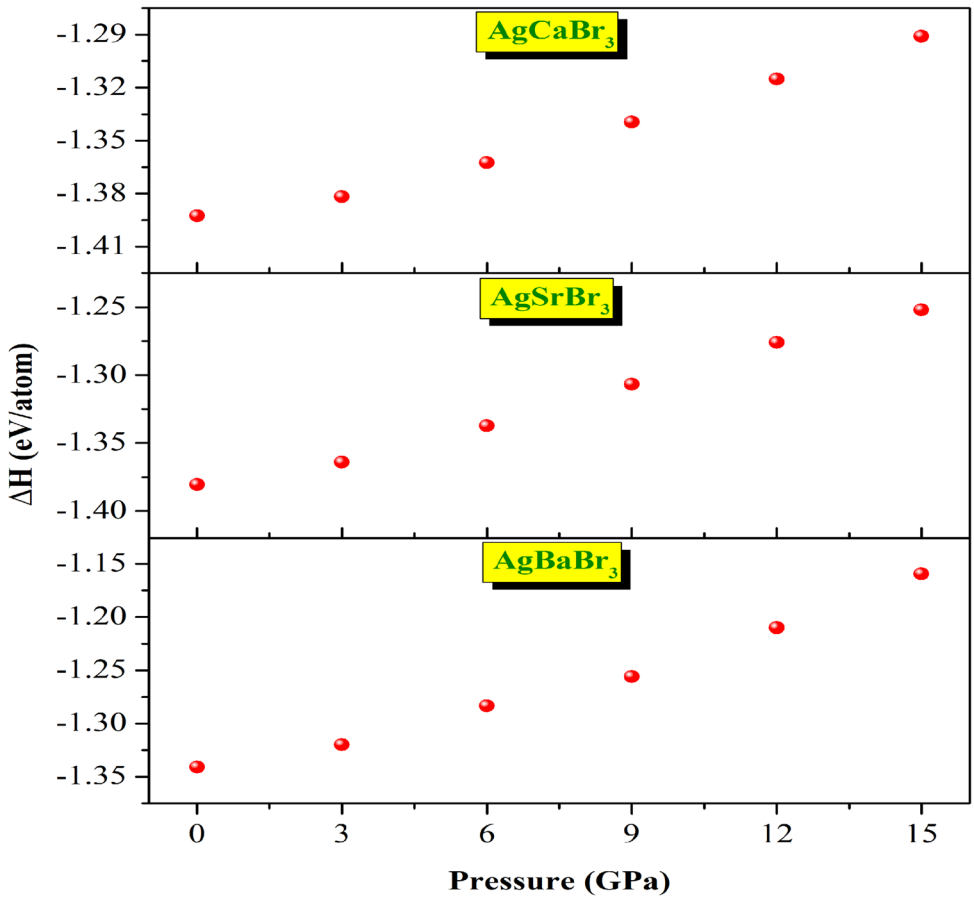

Fig. 2 Pressure dependence of the enthalpy of formation (ΔH) for $AgCaBr_3$, $AgSrBr_3$ and $AgBaBr_3$ materials

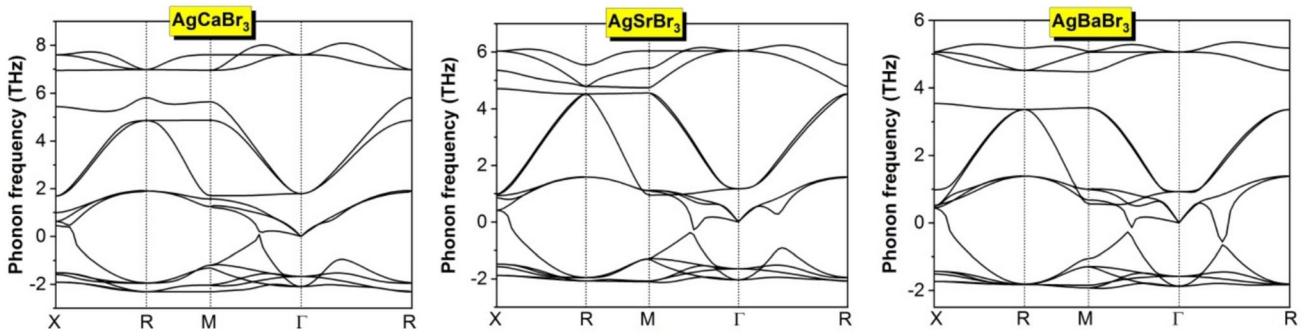

Fig. 3 Phonon dispersion curves for $AgCaBr_3$, $AgSrBr_3$ and $AgBaBr_3$ compounds

correlation functionals are listed in Table 2. It is clear from Table 2 that the band gap values obtained using the GGA-PBE exchange–correlation functional are remarkably smaller compared to the corresponding values obtained using the TB-mBJ and HSE06 functionals. It is widely recognized that the GGA functional tends to underestimate the value of the band gap. It is worth mentioning that the band gap values produced using GGA-PBEsol show a higher degree of agreement with those documented in previous studies that used DFT with the GGA functional. [34]. The TB-mBJ and HSE06 exchange–correlation functionals produce significantly improved bandgap values compared to those obtained using GGA-PBEsol. Examination of the calculated band structures determined using the TB-mBJ potential indicates that all three compounds studied have fundamental indirect energy band gaps (Γ–R) of approximately 4 eV, with a slight increase as the atomic size of element X increases from $AgCaBr_3$ to $AgSrBr_3$ to $AgBaBr_3$. Based on the calculated values of the energy bandgaps, these compounds can be classified as wide

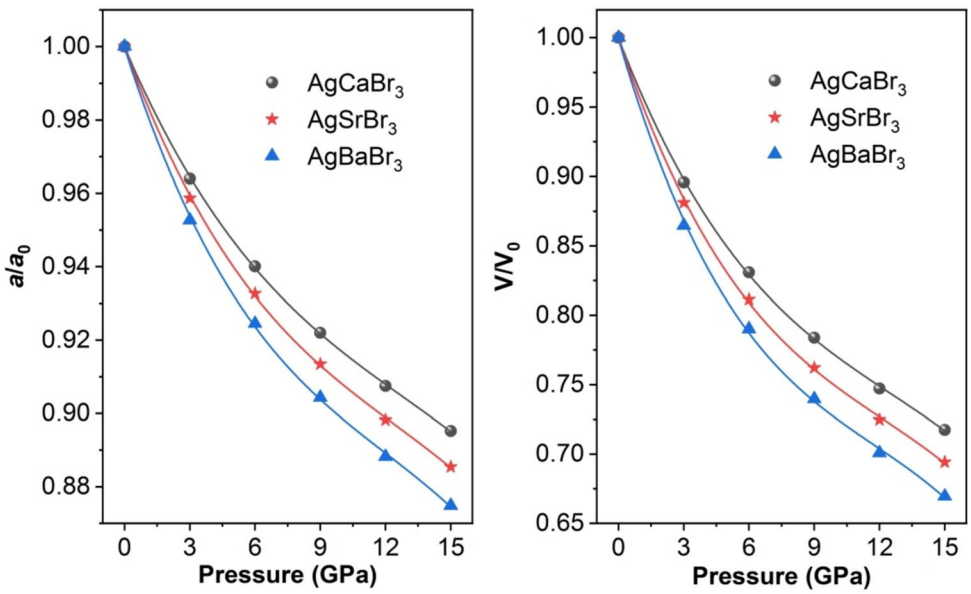

Fig. 4 Pressure dependence of a/a_0 and V/V_0 for $AgCaBr_3$, $AgSrBr_3$ and $AgBaBr_3$ materials. a and V are the lattice parameter and unit cell volume, respectively, at a pressure P and a_0 and V_0 are their corresponding values, respectively, at zero pressure

Table 2 The predicted values (in eV) of the energy direct bandgap R–R and indirect bandgaps Γ–R and X–R using the GGA-PBEsol, TB-mBJ and HSE06 functionals for $AgCaBr_3$, $AgSrBr_3$ and $AgBaBr_3$ compounds and the relevant theoretical information found in existing literature

Compound	XC functional	*R–R*	*Γ–R*	*X–R*
$AgCaBr_3$	GGA-PBEsol	1.189	0.809	0.823
$AgSrBr_3$	TB-mBJ	4.308	3.986	4.002
$AgBaBr_3$	HSE06	1.061	2.321	0.797
	Other [34]	4.386	0.730	4.144
	GGA-PBEsol	0.817	0.790	0.694
	TB-mBJ	4.410	4.143	4.295
	HSE06		2.285	
	Other [34]		0.730	
	GGA-PBEsol		0.689	
	TB-mBJ		4.292	
	HSE06		2.174	
	Other [34]		0.640	

bandgap semiconductors, and this makes them potential candidates for ultraviolet and visible light emitters, transparent conducting electrode and other optoelectronic applications [62–64]. It is worth noting that Table 2 and Fig. 6 show that the values of the R–R and X–R energy band gaps, especially that of the X–R band gap, are quite close to that of the fundamental band gap.

To analyze the nature and distribution of the electronic states forming the energy bands of the $AgXBr_3$ compounds, we calculated the total density of states (TDOS) and the partial density of states (PDOS) on specific atomic sites and orbitals within an energy range of −15 to 10 eV. Figure 7 displays the calculated TDOD and PDOS curves. The obtained DOS diagrams reveal that the characteristics of the DOS spectra of the compounds considered are similar. This similarity can be attributed to the fact that the differing atoms, X (X = Ca, Sr, or Ba), are isoelectronic. Figure 7 shows that the valence bands of $AgCaBr_3$ are subdivided into two distinct subbands, V1 and V2, while for $AgSrBr_3$ and $AgBaBr_3$, the valence bands are subdivided into three band groups: V1, V2, and V3. The lowest energy valence band groups of $AgSrBr_3$ and $AgBaBr_3$, labeled V3, exhibit relatively narrow shapes with peaks centered at −15 eV and −12.61 eV, respectively. Similarly, the V2 valence subband, which also has narrow shapes, shows a peak centered at −12.61 eV for $AgCaBr_3$, −12.17 eV for $AgSrBr_3$, and −9.67 eV for $AgBaBr_3$. All of these valence band groups, namely V2 and V3, are composed of hybridized Br-*s* and X-*p* (X = Ca, Sr, or Ba) states. The upper valence band groups extend from −2.80 eV, −2.21 eV, and −2.07 eV to the Fermi level (0 eV) for $AgCaBr_3$, $AgSrBr_3$, and AgBaBr3, respectively.

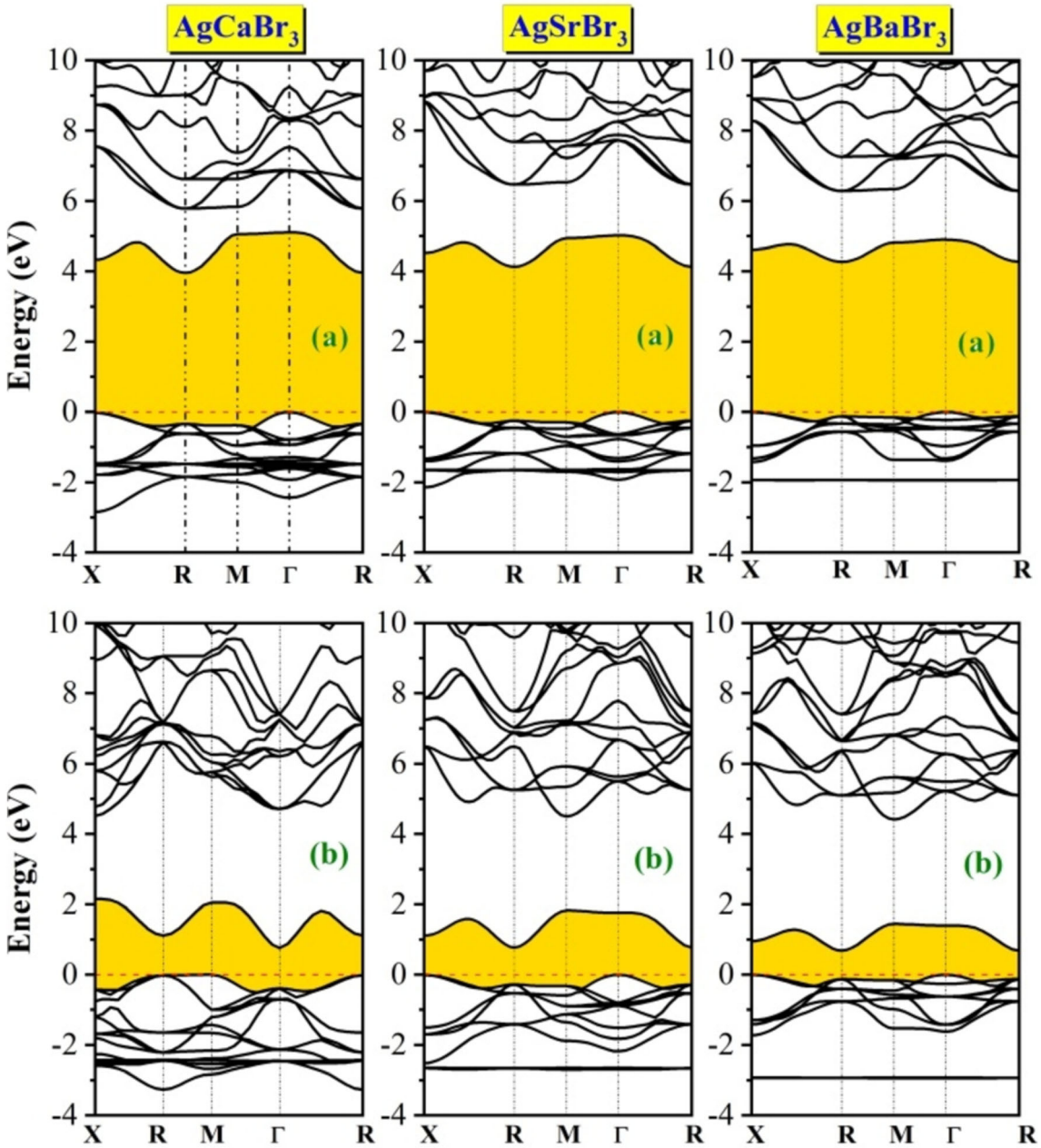

Fig. 5 Band energy dispersions along the high-symmetry directions as calculated using the FP-LAPW + lo method with the TB-mBJ (**a**) and GGA-PBEsol (**b**) functionals for $AgCaBr_3$, $AgSrBr_3$ and $AgBaBr_3$ materials. The Fermi level is shifted to zero

This valence subband is mainly formed by the hybridization between the *d* orbitals of Ag atoms and the *p* orbitals of Br atoms. The *p* orbitals of Ca, Sr, and Ba atoms are primarily responsible for the bottom of the conduction band.

3.3. Optical properties

An investigation was conducted to examine the optical characteristics of $AgCaBr_3$, $AgSrBr_3$, and $AgBaBr_3$ compounds within the energy range of 0–30 eV. This theoretical investigation was undertaken to analyses the optical properties by examining the frequency-dependent dielectric function, represented as $\varepsilon(\omega) = \varepsilon_1(\omega) + i\varepsilon_2(\omega)$. The absorption events occurring within the crystal are characterized by the imaginary component $(\varepsilon_2(\omega))$ of the dielectric function, which may be determined using the electronic band structure data. The Kramer-Kronig transformation can be used to get the real component $(\varepsilon_1(\omega))$ of the dielectric function, which characterizes the scattering

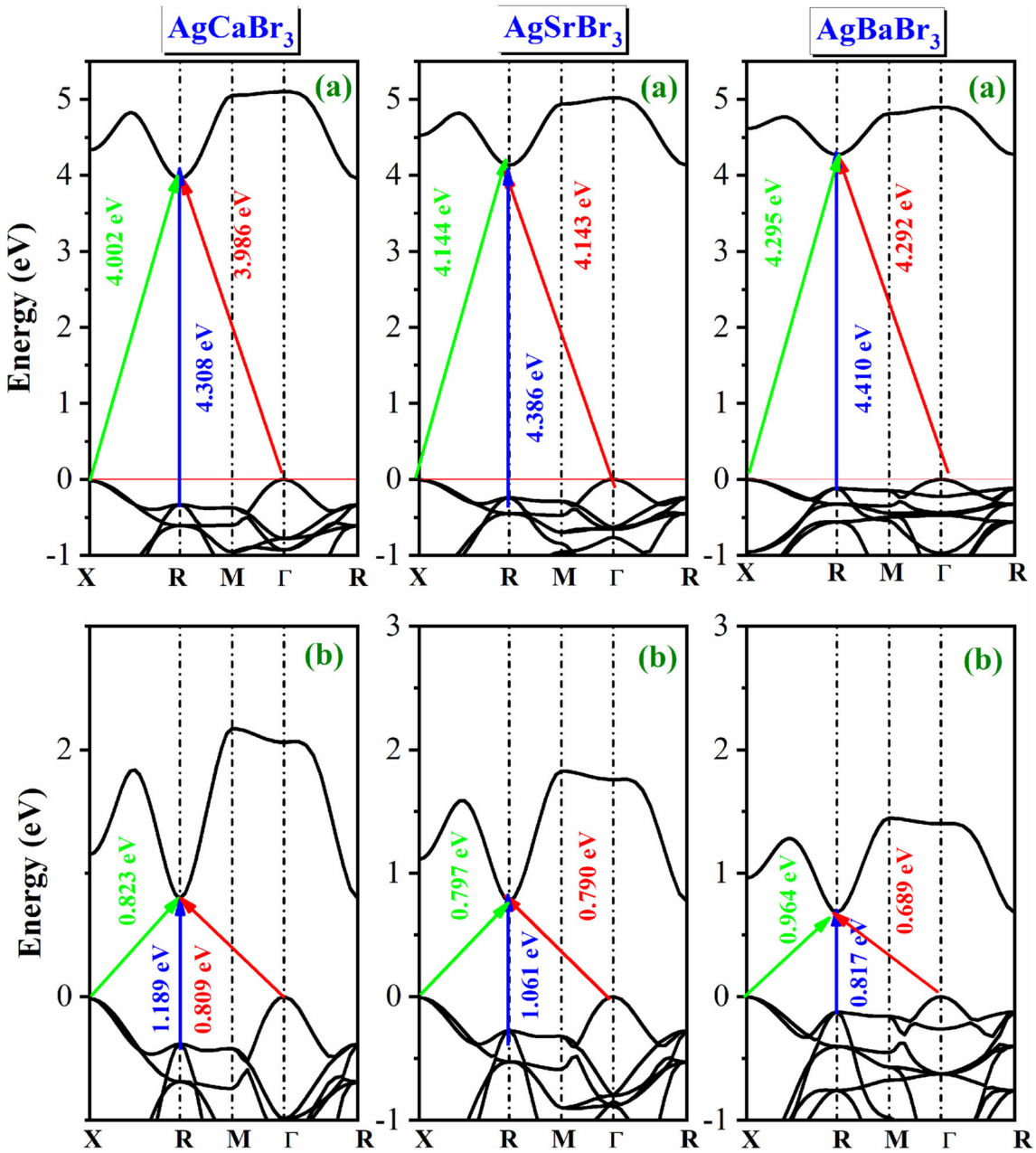

Fig. 6 Enlarged view of the band structure around the fundamental band gap with indication of the values of energy bandgaps Γ–R, R–R and X–R for $AgCaBr_3$, $AgSrBr_3$, and $AgBaBr_3$ materials

of electromagnetic radiation upon its entry into a medium [65]. The frequency-dependent imaginary and real components of the dielectric function for the materials under investigation are depicted in Fig. 8. The determination of the static dielectric constant occurs at the lower energy limit, which is represented as $\varepsilon(0) = \varepsilon_1(\omega \to 0)$ [44, 66]. The static dielectric constants of $AgCaBr_3$, $AgSrBr_3$, and $AgBaBr_3$ are measured to be 2.88, 2.61, and 2.48, respectively. The findings align with the Penn model [67]: $\varepsilon(0) \approx \hbar\omega_p/E_g^2$, where $\hbar\omega_p$ represents the plasma energy. In other words, a reduction in E_g corresponds to an increase in $\varepsilon(0)$.

The primary purpose is to determine the origins of electronic transitions that contribute to the structures visible in the $\varepsilon_2(\omega)$ spectrum. This involves the identification of the particular energy bands implicated, namely the valence band V_i and the conduction band C_j, together with the electronic states that are engaged in these transitions. The methodology entails the isolation of electronic transitions that take place between each pair of energy bands

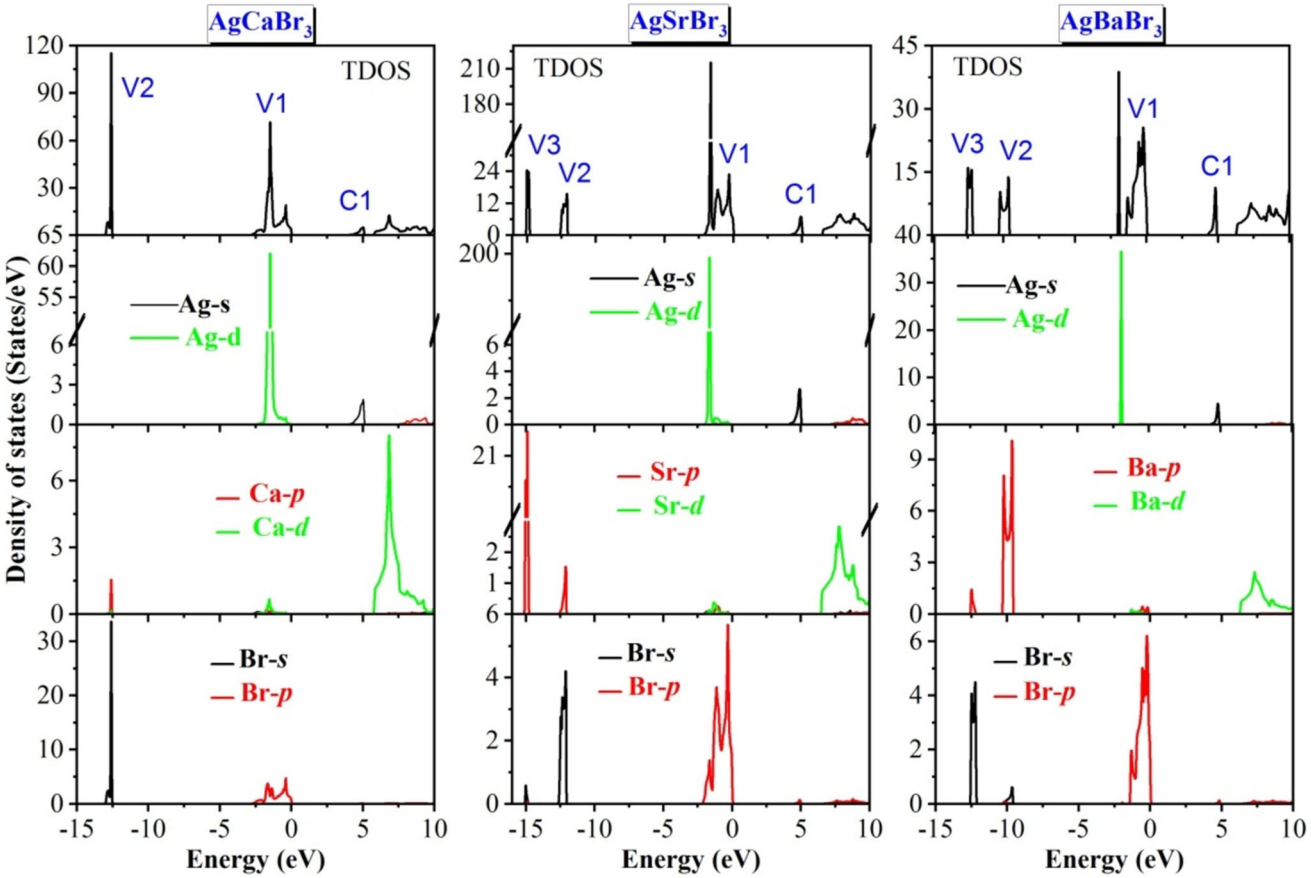

Fig. 7 Total density of state (TDOS) and *l*-decomposed site projected density of states (PDOS) for $AgCaBr_3$, $AgSrBr_3$, and $AgBaBr_3$ materials as calculated using the TB-mBJ potential. The energy zero (0 eV) is chosen to be at the Fermi energy

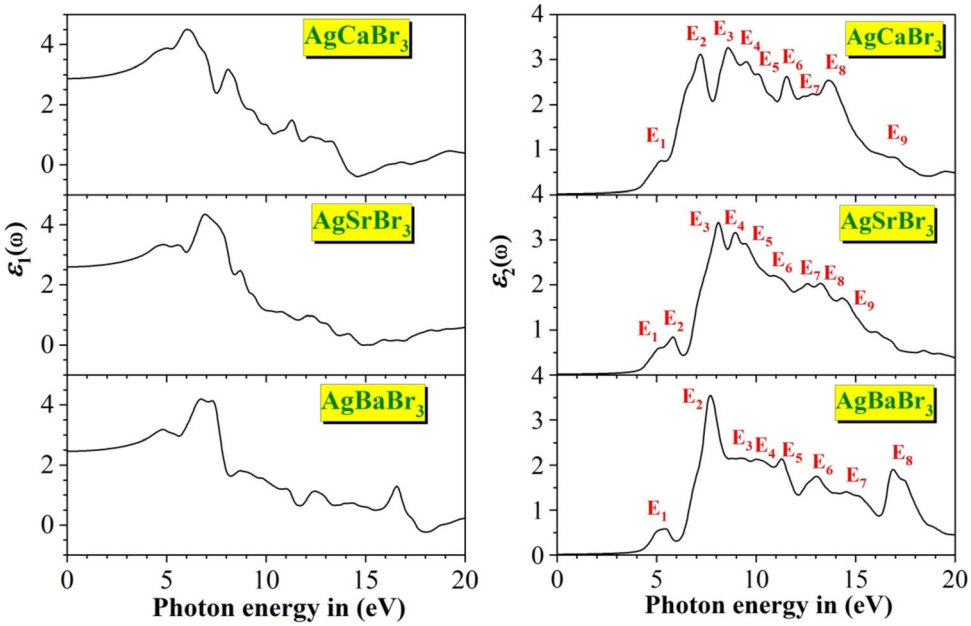

Fig. 8 The spectra of the real ($\varepsilon_1(\omega)$) and imaginary ($\varepsilon_2(\omega)$) parts of the dielectric function for $AgCaBr_3$, $AgSrBr_3$, and $AgBaBr_3$ compounds. The calculations were performed using the TB-mBJ potential

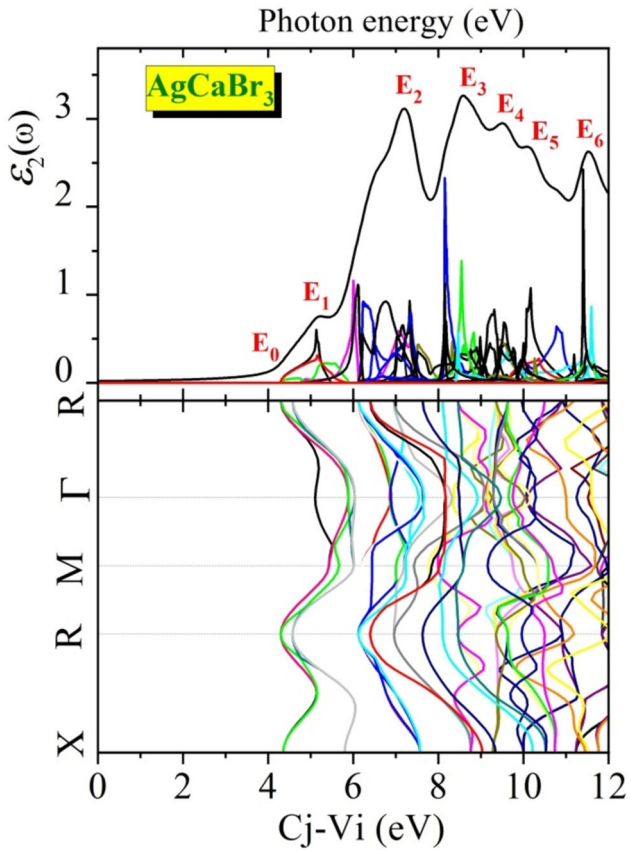

Fig. 9 Decomposition of the spectrum of the imaginary part $\varepsilon_2(\omega)$ of the dielectric function into band-to-band contributions (top panel) and the transition energy band structure (bottom panel) for $AgCaBr_3$

$V_i \rightarrow C_j$, together with their corresponding contributions. The identification of electronic states that primarily contribute to this process is facilitated by the electronic transition energy bands: $(E(C_j) - E(V_i))(k)$. Consequently, there exists a correlation between peak energies and electronic energy transitions. In the upper panel of Fig. 9, the notable contributions of interband electronic transitions are illustrated for $AgCaBr_3$, which serves as prototype. Furthermore, the lower panel of Fig. 9 shows the locations of the electronic states (that contribute to the electronic transitions) in the Brillouin zone (BZ) that for the three materials under investigation. The initial pivotal point E_0 of the curve represents the optical absorption threshold. The energy band pairings (V_i, C_j) and the positions in the Brillouin zone (BZ) of electronic states that are principally responsible for the formation of the spectra are presented in Tables S1, S2 and S3.

Figure 10 displays the spectra of the absorption coefficients $\alpha(\omega)$, refractive index $n(\omega)$, extinction coefficient $k(\omega)$, electron energy loss $L(\omega)$, and reflectivity $R(\omega)$ for the materials $AgCaBr_3$, $AgSrBr_3$, and $AgBaBr_3$, as functions of incident photon energy. A significant absorption is seen throughout a broad energy range spanning from approximately 3.9 to 42 eV for $AgCaBr_3$, 4.16 to 41 eV for $AgSrBr_3$, and 4.11 to 40.7 eV for $AgBaBr_3$. The compounds $AgCaBr_3$, $AgSrBr_3$ and AgBaBr3 exhibit maximum absorption intensities at approximately 27.1 eV, 22.8 eV and 17.7 eV, respectively. These compounds possess the ability to absorb light within the ultraviolet range and demonstrate transparency within the visible spectrum. As a result, they may serve as efficient filters for a wide array of radiation intensities, encompassing the ultraviolet (UV) spectrum. At energy levels above 42 eV, the transparency of these compounds is observed as a result of a gradual decline in electron reactivity.

The refractive index $n(\omega)$ is an essential optical parameter that quantifies the degree of bending of electromagnetic radiation in a given medium [68]. The $n(\omega)$ curve exhibits a consistent trend at lower energy levels, progressively rising as energy near the absorption edge, reaching its highest point before decreasing at higher energy levels. The greatest refractive index values observed for $AgCaBr_3$, $AgSrBr_3$, and $AgBaBr_3$ are 2.14, 2.09, and 2.11, respectively, when exposed to photons of energy levels of 6.11 eV, 7.39 eV, and 7.45 eV, respectively. The static refractive index $n(0)$ of $AgCaBr_3$, $AgSrBr_3$, and $AgBaBr_3$ demonstrates an upward tendency, in contrast to the decreasing behavior of the bandgap. In addition, it is worth noting that each compound exhibits distinct energy levels at which the extinction coefficient $k(\omega)$ reaches its highest value. Specifically, $AgCaBr_3$ exhibits a peak value of 1.11 at 13.87 eV, $AgSrBr_3$ reaches a peak value of 0.95 at 9.58 eV, and $AgBaBr_3$ reaches a peak value of 0.96 at 7.88 eV.

The materials under consideration have a markedly low static optical reflectivity, with values of 6.7% for $AgCaBr_3$, 5.3% for $AgSrBr_3$, and 4.6% for $AgBaBr_3$. The electron energy loss function ($L(\omega)$) is essential for comprehending the dissipation of energy when high-velocity electrons move through a substance [69]. The $L(\omega)$ spectra of $AgCaBr_3$, $AgSrBr_3$ and $AgBaBr_3$ compounds exhibit plasmon peaks at approximately 27.79 eV, 24.09 eV and 19.45 eV, respectively.

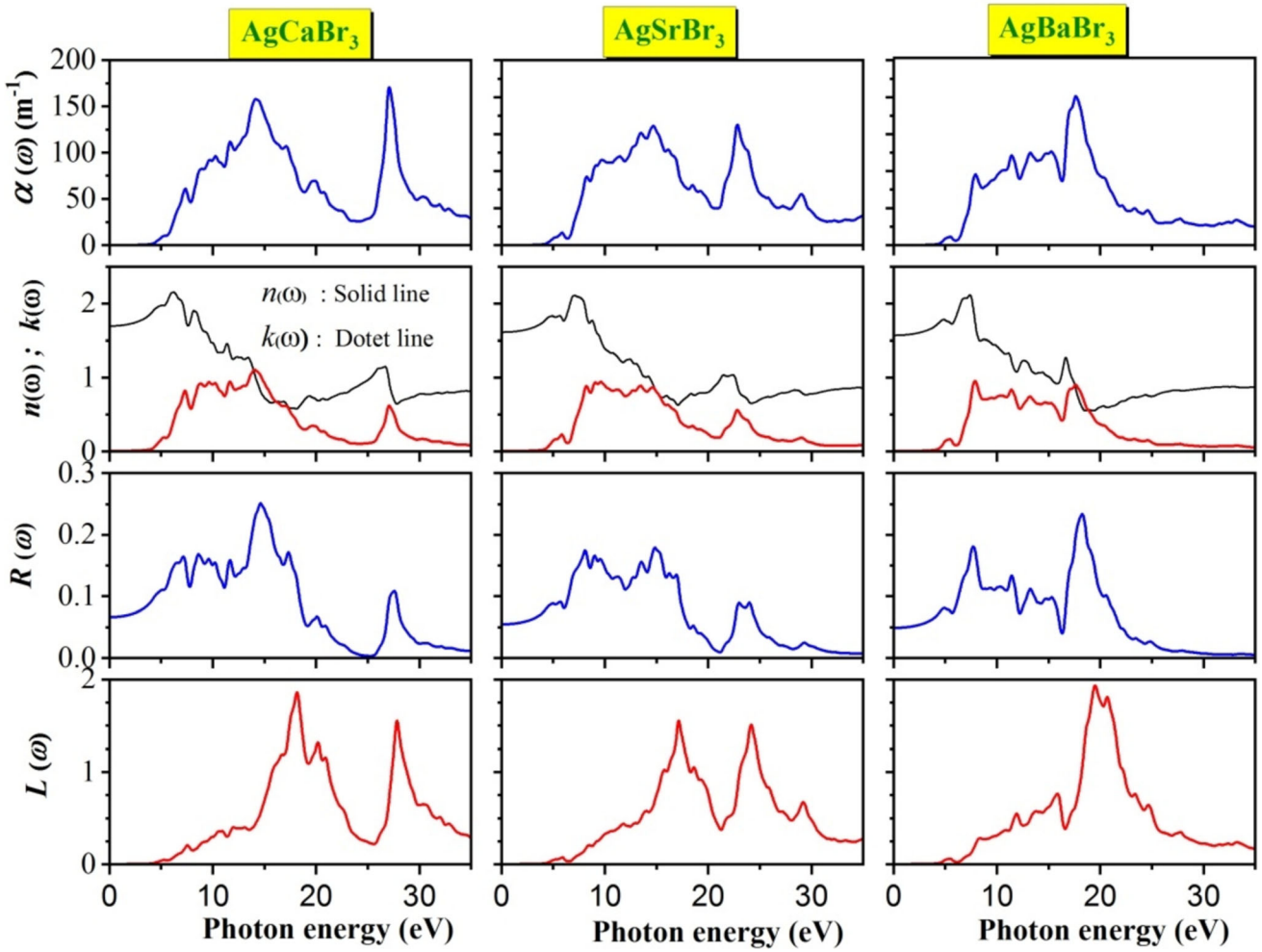

Fig. 10 The calculated spectra of the absorption coefficient α(ω), refractive index $n(\omega)$, extinction coefficient $k(\omega)$, optical reflectivity $R(\omega)$ and electron energy loss function $L(\omega)$ for $AgCaBr_3$, $AgSrBr_3$ and $AgBaBr_3$ compounds as calculated using the TB-mBJ potential

4. Conclusion

The present study employed the full potential augmented plane wave plus local orbitals approach to examine the structural, electronic and optical characteristics of the cubic perovskite $AgXBr_3$, where X is Ca, Sr, or Ba. The exchange–correlation interactions were described using three different functionals, specifically GGA-PBEsol, TB-mBJ and HSE06. The results of our study indicate that all three materials demonstrate semiconducting properties. $AgCaBr_3$, $AgSrBr_3$, and $AgBaBr_3$ have an indirect bandgap located between the Γ and R points in BZ. The bandgap values of $AgCaBr_3$, $AgSrBr_3$, and $AgBaBr_3$ using the TB-mBJ (HSE06, GGA-PBEsol) functional are 3.986 (2.321, 0.809), 4.143 (2.321, 0.790), and 4.292 (2.174, 0.689) eV, respectively. Calculations of dielectric functions and their associated optical characteristics, such as extinction coefficient, refractive index, absorption coefficient, electronic energy loss function, and reflectivity, have been performed over a broad energy spectrum from 0 to 35 eV. Significant absorption is observed across a broad energy range spanning from approximately 3.9 to 42 eV for $AgCaBr_3$, 4.16 to 41 eV $AgSrBr_3$, and 4.11 to 40.7 eV $AgBaBr_3$. Accordingly, these compounds are capable of absorbing light in the ultraviolet range while maintaining transparency in the visible spectrum. Consequently, they function as effective filter for a wide array of radiation intensities, encompassing the far ultraviolet (UV) spectrum. Additionally, valuable insights into the microscopic origins of the properties of optical spectra were achieved by decomposing the imaginary part of the dielectric function into contributions of different band-to-band transitions and developing transition band structures. Moreover, this methodology facilitated the distinction of contributions originating from various places inside the Brillouin zone. Notably, a rise in the value of the static dielectric constant $\varepsilon(0)$ was seen when the bandgap (E_g) decreased, aligning with the predictions made by the Penn model.

References

[1] U-G Jong, C-J Yu, Y-H Kye, Y-G Choe, W Hao and S Li *Inorg. Chem.* **58** 4134 (2019).
[2] J-H Lee, Z Deng, N C Bristowe and P D Bristowe *J. Mater. Chem. C* **6** 12252 (2018).
[3] A Kojima, K Teshima and Y Shirai *J. Am. Chem. Soc.* **131** 6050 (2009).
[4] H-S Kim, C-R Lee, J-H Im, K-B Lee, T Moehl, A Marchioro, S-J Moon, R Humphry-Baker, J-H Yum and J E Moser *Sci. Rep.* **2** 591 (2012).
[5] J Tong, Z Song, D H Kim, X Chen, C Chen, A F Palmstrom, P F Ndione, M O Reese, S P Dunfield, O G Reid, J Liu, F Zhang, S P Harvey, Z Li, S T Christensen, G Teeter, D Zhao, M M Al-Jassim, M F A M Van Hest et al *Science* **364** 475 (2019).
[6] Md Z Rahaman and M A Islam *J. Supercond. Nov. Magn.* **34** 1133 (2021)
[7] T Yi, W Chen, L Cheng, R D Bayliss, F Lin, M R Plews, D Nordlund, M M Doeff, K A Persson and J Cabana *Chem. Mater.* **29** 1561 (2017).
[8] N S Arul and V D Nithya (eds) *Revolution of Perovskite: Synthesis, Properties and Applications* (Singapore: Springer Singapore) (2020)
[9] G H Haertling *J. Am. Ceram. Soc.* **82** 797 (1999).
[10] N Setter and E L Colla (eds) *Ferroelectric Ceramics: Tutorial reviews, theory, processing, and applications* (Basel : Birkhäuser Basel) (1993)
[11] A Bedjaoui, D Allali, M Radjai, A Bouhemadou, S S Essaoud, S Bin-Omran, R Khenata and Y Al-Douri *Solid State Commun.* **387** 115532 (2024).
[12] L E Cross and R E Newnham *Ceram. Civiliz.* **3** 289 (1987).
[13] H Jaffe *J. Am. Ceram. Soc.* **41** 494 (1958).
[14] F J Loureiro, N Nasani, G S Reddy and N R Munirathnam *J. Power Sources* **438** 226991 (2019).
[15] A S Bhalla, R Guo and R Roy *Mater. Res. Innov.* **4** 3 (2000).
[16] P Gao, M Grätzel and M K Nazeeruddin *Energy Environ. Sci.* **7** 2448 (2014).
[17] M A Riza, M A Ibrahim, U C Ahamefula, M A M Teridi, N A Ludin, S Sepeai and K Sopian *Sol. Energy* **137** 371 (2016).
[18] M Liu, M B Johnston and H J Snaith *Nature* **501** 395 (2013).
[19] I Chung, B Lee, J He, R P Chang and M G Kanatzidis *Nature* **485** 486 (2012).
[20] G Natta *Rend Accad Naz Lincei* **5** 1003 (1927).
[21] C P Brock *Acta Crystallogr. Sect. A* **64** C167 (2008).
[22] Y Zhao and K Zhu *Chem. Soc. Rev.* **45** 655 (2016).
[23] N Sarukura, H Murakami, E Estacio, S Ono, R El Ouenzerfi, M Cadatal, T Nishimatsu, N Terakubo, H Mizuseki and Y Kawazoe *Opt. Mater.* **30** 15 (2007).
[24] F Zhang, Y Mao, T-J Park and S S Wong *Adv. Funct. Mater.* **18** 103 (2008).
[25] D Babel *Structural chemistry of octahedral fluorocomplexes of the transition elements* (eds) C K Jørgensen, J B Neilands, R S Nyholm, D Reinen, and R J P Williams, (Berlin, Heidelberg : Springer Berlin Heidelberg) p 1 (1967)
[26] J Lu, S-C Chen and Q Zheng *ACS Appl. Energy Mater.* **1** 5872 (2018).
[27] S Cheng, Q Chang, Z Wang, L Xiao, E E M Chia and H Sun *Adv. Opt. Mater.* **9** 2100564 (2021).
[28] N L Allan, M J Dayer and D T Kulp *J. Mater. Chem.* **1** 1035 (1991).
[29] P Hagenmuller *Inorganic solid fluorides: chemistry and physics* (Elsevier) (2012).
[30] J W Fergus *Sens. Actuators B Chem.* **42** 119 (1997).
[31] I J Videau and I Portier *Inorg. Solid Fluorides Chem. Phys.* **309** (1985)
[32] S S Essaoud, S M Al Azar, A A Mousa and R S Masharfe *Phys. Scr.* **98** 035820 (2023).
[33] S G Motti, D Meggiolaro, S Martani, R Sorrentino, A J Barker, F De Angelis and A Petrozza *Adv. Mater.* **31** 1901183 (2019).
[34] J I Gómez-Peralta and X Bokhimi *Mater. Chem. Phys.* **267** 124710 (2021).
[35] J I Gómez-Peralta and X Bokhimi *J. Solid State Chem.* **285** 121253 (2020).
[36] P Blaha, K Schwarz, F Tran, R Laskowski and G K Madsen *J. Chem. Phys.* **152** 074101 (2020).
[37] F Tran and P Blaha *Phys. Rev. Lett.* **102** 226401 (2009).
[38] S Cottenier *Inst. Voor Kern-En Stralingsfysica KU Leuven Belg.* **4** 41 (2002)
[39] H J Monkhorst and J D Pack *Phys. Rev. B* **13** 5188 (1976).
[40] J P Perdew, A Ruzsinszky, G I Csonka, O A Vydrov, G E Scuseria, L A Constantin, X Zhou and K Burke *Phys. Rev. Lett.* **100** 136406 (2008).
[41] J Heyd and G E Scuseria *J. Chem. Phys.* **121** 1187 (2004).
[42] A V Krukau, O A Vydrov, A F Izmaylov and G E Scuseria *J. Chem. Phys.* (2006). https://doi.org/10.1063/1.2404663
[43] J Heyd and G E Scuseria *J. Chem. Phys.* **118** 8207 (2003).
[44] K M Wong, W Khan, M Shoaib, U Shah and S H Khan *J. Electron. Mater.* **47** 566 (2018).
[45] F D Murnaghan *Proc. Natl. Acad. Sci.* **30** 244 (1944)
[46] C Li, X Lu, W Ding, L Feng, Y Gao and Z Guo *Acta Crystallogr. B* **64** 702 (2008).
[47] Y Pan and F Yang *J. Energy Storage* **87** 111492 (2024).
[48] Y Pan *Inorg. Chem.* **63** 8264 (2024).
[49] Y Pan and Z Yang *J. Hydrog. Energy* **82** 1308 (2024).
[50] J Zhu and Y Pan *Mater. Sci. Eng. B* **308** 117554 (2024).
[51] Y Pan and M Wen *J. Am. Ceram. Soc.* **107** 1081 (2024).
[52] M D Segall and P J Lindan *J. Phys. Condens. Matter* **14** 2717 (2002).
[53] D V Suetin and I R Shein *Phys. Solid State* **60** 213 (2018).
[54] C-Y Yoo, K-P Hong and S-J Kim *Acta Crystallogr. C* **63** i63 (2007).
[55] Y Pan *Int. J. Refract. Met. Hard Mater.* **121** 106676 (2024).
[56] Y Pan *Mater. Today Chem.* **35** 101915 (2024).
[57] Y Pan and F Yang *Ceram. Int.* **50** 14856 (2024).
[58] Y Pan and J Zhu *Mater. Today Commun.* **38** 108428 (2024).
[59] Y Pan and J Zhu *Vacuum* **225** 113242 (2024).
[60] A Gherriche, A Bouhemadou, Y Al-Douri, S Binomran, R Khenata and M Hadi *Mater. Sci. Semicond. Process.* **131** 105890 (2021).
[61] K Omri, I Najeh and L El Mir *Ceram. Int.* **42** 8940 (2016).
[62] K Omri, I Najeh, S Mnefgui, N Alonizan and S Gouadria *Mater. Sci. Eng. B* **297** 116738 (2023).
[63] K Omri, A Bettaibi and K Khirouni *B Condens. Matter* **537** 167 (2018).
[64] K Omri and N Alonizan *J. Mater. Sci. Mater. Electron.* **33** 15448 (2022).
[65] A Bouhemadou, S Bin-Omran, D Allali, S M Al-Otaibi, R Khenata, Y Al-Douri, M Chegaar and A H Reshak *Mater. Res. Bull.* **64** 337 (2015).
[66] A Bouhemadou, S Al-Essa, D Allali, M A Ghebouli and S Bin-Omran *Solid State Sci.* **20** 127 (2013).
[67] D R Penn *Phys. Rev.* **128** 2093 (1962).

[68] C A Mead *Phys. Rev.* **128** 2088 (1962).
[69] D Allali, A Bouhemadou, E M A Al Safi, S Bin-Omran, M Chegaar, R Khenata, and A H Reshak *Phys. B Condens. Matter* **443** 24 (2014)